RESEARCH ARTICLE | JUNE 29 2023

Inelastic scattering of OH from a liquid PFPE surface: Resolution of correlated speed and angular distributions

Maksymilian J. Roman ; Adam G. Knight ; Daniel R. Moon ; Paul D. Lane ; Stuart J. Greaves ;
Matthew L. Costen ; Kenneth G. McKendrick

Check for updates

View Online   Export Citation   CrossMark

Articles You May Be Interested In

Non-equilibrium responses of PFPE lubricants with various atomistic/molecular architecture at elevated temperature

AIP Advances (March 2017)

Characterization of Perfluorinated Polyether (PFPE) Disk Drive Lubricants

Surface Science Spectra (October 1996)

Deposition of perfluoropolyether lubricant films on Si-incorporated diamondlike carbon surfaces

J. Appl. Phys. (April 2006)

Inelastic scattering of OH from a liquid PFPE surface: Resolution of correlated speed and angular distributions

View Online   Export Citation   CrossMark

Maksymilian J. Roman, [ID] Adam G. Knight, [ID] Daniel R. Moon, [ID] Paul D. Lane, [ID] Stuart J. Greaves, [ID]
Matthew L. Costen, [ID] and Kenneth G. McKendrick[a) [ID]

AFFILIATIONS

Institute of Chemical Sciences, Heriot-Watt University, Edinburgh EH14 4AS, United Kingdom

[a)]Author to whom correspondence should be addressed: k.g.mckendrick@hw.ac.uk

ABSTRACT

Inelastic collisions of OH with an inert liquid perfluoropolyether (PFPE) surface have been studied experimentally. A pulsed molecular beam of OH with a kinetic energy distribution peaking at 35 kJ mol^{-1} was directed at a continually refreshed PFPE surface. OH molecules were detected state-selectively with spatial and temporal resolution by pulsed, planar laser-induced fluorescence. The scattered speed distributions were confirmed to be strongly superthermal, regardless of the incidence angle (0° or 45°). Angular scattering distributions were measured for the first time; their reliability was confirmed through extensive Monte Carlo simulations of experimental averaging effects, described in Paper II [A. G. Knight *et al.*, J. Chem. Phys. **158**, 244705 (2023)]. The distributions depend markedly on the incidence angle and are correlated with scattered OH speed, consistent with predominantly impulsive scattering. For 45° incidence, the angular distributions are distinctly asymmetric to the specular side but peak at sub-specular angles. This, along with the breadth of the distributions, is incompatible with scattering from a surface that is flat on a molecular scale. New molecular dynamics simulations corroborate the roughness of the PFPE surface. A subtle but unexpected systematic dependence of the angular distribution on the OH rotational state was found, which may be dynamical in origin. The OH angular distributions are similar to those for kinematically similar Ne scattering from PFPE and hence not strongly perturbed by OH being a linear rotor. The results here are broadly compatible with prior predictions from independent quasiclassical trajectory simulations of OH scattering from a model-fluorinated self-assembled monolayer surface.

INTRODUCTION

Scattering of molecules at the gas–liquid interface is of central importance in a wide range of natural and technological processes, including gas uptake and sequestration, multiphase catalysis, respiration, and atmospheric chemistry.[1–5] Fundamental dynamical studies of scattering at the gas–liquid interface are, therefore, highly desirable to understand the mechanisms by which molecules react or are accommodated at liquid surfaces. However, despite recent progress, they remain relatively underdeveloped compared with much more extensive work on gas-phase or gas–solid surface scattering.[6,7]

In the context of atmospheric chemistry, aerosol particles represent, by far, the most-extensive overall liquid-surface area exposed to gas-phase molecules. These surfaces are "aged" by gas-phase oxidants, with important climatic consequences through the effects on radiative balance and cloud condensation.[8] A major contribution is made by the OH radical,[9] whose collisions at the gas–liquid interface are the specific focus of this work. Recent studies of model epithelial lung fluids have also shown that interfacial reactions of OH may play a role in the adverse health effects of breathing polluted air containing O_3 and other oxidants.[10,11] The majority of the previous effort on OH in gas–liquid systems has been focused on the reactive loss or uptake coefficient.[12–18] In this work, we address the complementary information contained in the dynamical attributes (speed, angular and internal-state distributions) of OH molecules that survive their encounter with the liquid and are scattered back into the gas phase.

18 September 2023 03:06:04

Interpretations of gas–liquid inelastic scattering mechanisms have largely been based around the limiting cases of "impulsive scattering" (IS) and "thermal desorption" (TD), originally introduced in the context of gas–solid scattering.[19,20] These lie at the opposite ends of a spectrum. The number of interactions with the surface is either unity or very small for IS, with the scattered-molecule attributes deterministically controlled by collision dynamics. In contrast, for TD, there are sufficiently many interactions that the outcome is uncorrelated with the initial conditions and determined purely by Maxwell-Boltzmann statistics reflecting the liquid temperature. These two limits are amenable to being distinguished experimentally. Depending on the incident kinetic energy, E_i, distinct differences in scattered speed distributions are obviously to be expected. We note also, in particular, the common preconception that IS distributions of the final angles, θ_f (with all angles measured from the normal), will be sharply directed in an approximately specular direction, in contrast to the $\cos(\theta_f)$-weighted distribution (Knudsen's law) expected for TD.[21,22] Simple, quantitative IS models, also originally developed in the context of gas–solid scattering, have been applied to gas–liquid scattering: "hard-cube" models allow, for a given incident angle, θ_i, the transfer from the vertical component of the initial momentum to an assumed flat surface of finite mass; "hard-sphere" versions incorporate scattering into a range of θ_f; and "soft-sphere" extensions include additional inelastic loss to other degrees of freedom.[6,23–29]

Beyond these limiting cases and simple models, detailed quasi-classical trajectory (QCT) calculations tend to reveal that the boundaries of the simple empirical separation into IS and TD categories are blurred.[7,30–36] For example, it is very common for some slower products to result from IS-like, single-bounce trajectories of superthermal incident molecules, and a number of identifiable sub-categories of temporary residence at the surface have been identified. The most directly relevant work of this type here is Troya's QCT study of interfacial OH scattering.[37] As is common in this field, a fluorinated self-assembled monolayer (F-SAM) was used as a proxy for a liquid surface, for reasons of computational convenience. The collision energy (E_i = 54 kJ mol^{-1}) was chosen to match our own earlier experiments on scattering of photolytically generated OH from liquid perfluoropolyether (PFPE), a prototypical inert surface that has been widely studied in related work.[38–40] A number of dynamical properties of the scattered OH were predicted; some, such as rotational distributions, could be compared against previous experiments, but others have been untested until the current work.

We report here new experimental measurements of OH scattering from liquid PFPE. We prepare the liquid surface using a partially immersed rotating wheel.[41] This relatively straightforward method has been widely adopted for low vapor-pressure liquids, such as PFPE.[6,7,42] We note in passing that it is not suitable for higher-vapor pressure liquids; although some such studies are beginning to emerge based on liquid microjets, these remain very challenging.[42–46]

The OH projectiles are generated using a molecular-beam (MB) source coupled to high-voltage discharge, which we have recently introduced into our experiments.[47] As demonstrated by extensive studies on the scattering of stable atoms or molecules, this has the advantage over photolytic methods of OH generation that θ_i is well-defined and can be varied by either rotating the surface relative to a fixed source or moving the source for a fixed surface, as we do here.

The most novel aspect of the approach here is the method of scattered-product detection. Broadly speaking, previous work on gas–liquid scattering can be divided between mass-spectrometric (MS) detection and some form of laser spectroscopy.[7] MS detection has the advantage of being "universal" and naturally well-adapted to measuring the speed (via time-of-flight, ToF) and angular distributions (by mechanical movement of the detector). We note, however, that there are important limitations on the range of angles that can be accessed due to physical constraints. There are no studies of OH inelastic scattering from liquid surfaces based on MS detection. The most directly relevant work is a series of earlier papers by Nathanson, Minton, and co-workers on the scattering of simple inert projectiles, including the noble gases, from PFPE and related liquids.[48–52]

Spectroscopic methods lack the universality of MS detection but are clearly uniquely capable of measuring internal-state distributions. It would be highly desirable to combine this aspect of spectroscopic detection with full resolution of speed and angular distributions, allowing new, mechanistically diagnostic correlations to be accessed. Of the principal spectroscopic methods in the gas–liquid scattering literature to date, IR absorption has so far only provided limited vectorial information, in part an intrinsic limit of a column-density measurement.[53–64] We note that in many related measurements in the gas phase, resonance-enhanced multiphoton ionization coupled with velocity map imaging (REMPI-VMI) would be the method of choice.[65] However, there are significant practical challenges to implement it for gas–liquid scattering.[66–72]

The other main method that has been applied so far to gas–liquid scattering is laser-induced fluorescence (LIF), including our own work on OH scattering using both photolytic and MB sources of OH.[38–40,47,73] Until recently, speed information from LIF had been confined in this context to ToF profiles obtained with a conventional narrow, cylindrical probe-laser beam.[47] It is also possible to get spatial information in this way, most simply by constraining the region from which the fluorescence is detected as in Zutz and Nesbitt's sequential pointwise measurements on NO scattering.[62] However, this requires laborious mechanical movement of optical components and has a spatial resolution limited by their design. In principle, there is a large multiplex advantage in measuring all positions simultaneously by expanding the probe laser beam into a sheet and taking an image of the emitted fluorescence, so-called planar LIF (pLIF). This idea has been widely exploited in other applications, especially in the imaging of combustion and to some extent of catalysis but sparingly in more-dynamical applications such as photodissociation.[74–80] To our knowledge, the only application of pLIF in a surface-scattering experiment is our own recent proof-of-concept report.[73] In essence, this involved taking a sequence of spatially resolved images as a function of delay between generation of the incoming molecular beam packet and the LIF probe pulse. We showed that it was possible to extract reliable information on the speeds of the OH molecules scattered from a liquid surface. However, experimental limitations prevented any clear conclusions about the angular scattering distributions.

Here, we present new and more incisive measurements of OH inelastic scattering from PFPE at a modestly superthermal OH collision energy of ~35 kJ mol^{-1} using a pLIF method that has been upgraded in important respects. In particular, we are able to measure the OH scattering angular distributions here for the first time. We have, in parallel, developed improved approaches to the analysis

18 September 2023 03:06:04

of the data and forward simulation of the results. In the companion paper,[81] henceforth "Paper II," we describe extensive Monte Carlo modeling that establishes how practical constraints affect the reliability of extracted speed or angular distributions; the general conclusions presented in this study are relevant well beyond this specific application of pLIF. The experimental results are compared with previous, kinematically similar measurements on other projectiles scattered from PFPE and with independent QCT predictions for OH scattered from an F-SAM proxy. We consider what information they contain about the molecular-level structure of the liquid PFPE surface, informed by new molecular dynamics (MD) predictions also carried out here, and reflect on what they imply about the applicability of the limiting-case IS and TD mechanisms.

EXPERIMENTAL

The majority of the experimental setup has been described previously;[47,73] however, several key changes and additions have been introduced for the work presented here. In summary, the main apparatus consisted of two stainless-steel vacuum chambers. The scattering experiments were carried out in the main chamber, whereas the load-lock chamber was used to store the liquids being studied. The chambers were evacuated by separate turbo pumps. When the molecular beam was operating, the pressure rose from its base value of low 10^{-6} mbar to low 10^{-5} mbar. This was more than adequate for the mean-free paths to be much longer than the distances traveled by the OH (the longest being 176.0 ± 0.5 mm from the source to the liquid surface).

Figure 1(a) shows a side-view schematic of the main chamber. A pulsed molecular beam valve was used to admit a mixture of ~3% H_2O seeded in 3 bar He through a 1 mm diameter nozzle into the main chamber. (There is a slight technical difference from our previous work where D_2O was used to produce an OD beam.[47,73]) A short (10 μs) high-voltage direct current discharge pulse in the high-pressure region at the exit of the valve created a packet of OH radicals embedded in a longer (nominally 300 μs) MB pulse.[47] The molecular beam was skimmed with a 2 mm diameter conical skimmer placed 40 mm downstream from the source. New to this work, a secondary collimator was placed a further 44 mm downstream. This consisted of an aluminum disk with a 3 mm diameter aperture, with a conical shape opening into a larger hole on the exit side. The resulting narrowing of the molecular-beam profile is one of the major improvements here over the previous studies.[47,73] It has a smaller transverse FWHM as measured at the observation zone (5.9 mm); the previous value was quoted as 7.1 mm but is now known to be closer to 10 mm following a more accurate recalibration of the absolute length scale (see below). Probably, at least as significantly for reasons that will emerge, the new molecular-beam profile also has substantially reduced intensity in the wings.

More details of the molecular-beam characterization and the modeling of the effects of geometric blurring due to its finite dimensions are given in Paper II.[81] We derive these quantitative estimates of the incident-angle- and scattering-angle-dependent corrections needed to account for the effects of the current finite beam (FB) dimensions on measured scattering angular distributions. Note that since they were defined in terms of integral ToF profiles through defined regions of interest (see below), it is not meaningful to apply them as a pixelwise correction to raw images; they are imposed during the process used to extract the angular distribution, as described below. The size of the FB correction is naturally larger as the
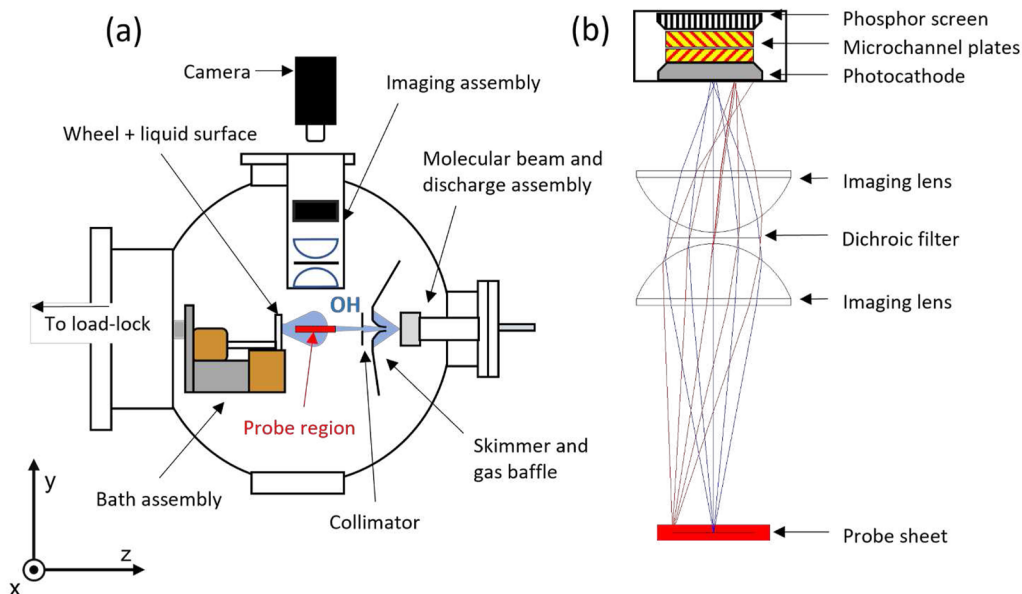
FIG. 1. (a) Schematic of the main chamber (not to scale); (b) close-up of the imaging assembly including indicative paths of fluorescence photons collected by the imaging lenses. The laser sheet was in the *xz* plane and propagated into the plane of the page (*x*-direction). The liquid-coated wheel lay in the *xy* plane and rotated about an axle along the *z*-direction. The MB propagated either along the surface normal, *z*, or at 45° to the surface normal in the *xz* plane.

incidence angle, θ_i, of the molecular beam increases (as measured as usual from the surface normal), due to the extension along one direction (the x-axis as defined here) of the dosed area on the surface. In this work, incidence angles of $\theta_i = 0°$ (i.e., along the surface normal) and 45° were used, achieved by mounting the entire MB assembly onto the main chamber via two different ports in the xz plane.

The OH packet has a spread of arrival times at the center of the observation region, due to the combined effects of spread of speeds and temporal width or spatial extent in the source. This resulted in a FWHM of 20.3 μs around the most-probable arrival time of 94.9 μs. The most-probable speed is 2050 m s^{-1}, corresponding to a most-probable laboratory-frame initial kinetic energy $E_i = 35$ kJ mol^{-1}, somewhat higher than our previous less-direct estimate (30 kJ mol^{-1}).[47,73] The speed was determined precisely by auxiliary measurements in which the source-probe region distance was varied—see supplementary material. The measured speed is slightly higher than that predicted (1751 m s^{-1}) from full conversion of the thermal energy in the supersonic expansion of the He carrier at room temperature,[82] suggesting some heating in the confined region as a result of the high-voltage discharge. The auxiliary measurements also revealed that the OH molecules took ~20 μs to traverse this region before flying freely toward the surface.

The addition of the collimator removed more of the outer, hotter part of the beam resulting in a rotationally colder beam of OH than we had seen previously for OD.[47,73] The rotational populations were well-described by a two-temperature fit, with $T_{rot,1} = 57 \pm 1$ and $T_{rot,2} = 164 \pm 1$ K and weighting parameter, $\alpha = 0.43 \pm 0.01$, indicating the proportion of the population with $T_{rot,1}$ (see supplementary material for the detailed rotational population distribution of OH in the beam). This corresponds to typically ~70% of the initial population being in the lowest level, $N = 1$.

As noted above, the liquid surface consisted of PFPE {Krytox® 1506, DuPont, F-[CF(CF$_3$)CF$_2$O]$_n$–CF$_2$CF$_3$, with mean $n = 14$—see Fig. 2}. A stainless-steel wheel rotated (~0.5 Hz) in a bath of the liquid, resulting in a continually refreshed, macroscopically flat surface oriented vertically (i.e., in the xy-plane) in the laboratory-frame. All measurements in this work were taken with the liquid at room temperature (298 K).

OH in $v = 0$ of the ground electronic state was probed on selected $Q_1(N)$ transitions [where N is as usual, the rotational quantum number excluding electron spin extrapolated from Hund's case (b) limit] of the A-X (1,0) band by excitation with pulsed tunable laser light in the wavelength range 282–283 nm.[38–40,47,73] As in our

most recent work, the probe beam was expanded into a sheet, but its spatial uniformity was significantly improved here, hence reducing variations in the OH detection efficiency (see below).[73] The revised optical design was conceptually similar, but differed in detail, to those described previously by others.[83] It consisted of two pairs of lenses, each in a telescope arrangement; the first pair were spherical lenses, expanding the beam radially, and the second cylindrical, collapsing it into a horizontal sheet. A square mask was placed between the telescopes to create sharper edges, within the limits of mode quality and diffraction effects. The resulting sheet had a rectangular cross section (~4 mm in the y-direction, and 30 mm in the z-direction, propagating along the x-direction in the laboratory-frame). It lay in the xz-plane containing the liquid-surface normal, directly in front of the central point of impact of the molecular beam [see Fig. 1(a)]. The z-distance between the liquid surface and the closest edge of the probe sheet was generally set to 10 mm, but could be adjusted by moving the beam-shaping optics for specific auxiliary measurements (see below).

The resulting pLIF signal was detected in the y-direction by the imaging assembly shown in Fig. 1(b). This has also been described in detail previously.[73] In essence, the combined assembly has the effect of collecting spatially resolved UV emission from a large viewing region efficiently with a small f number but with low distortion. The light is amplified by a large factor using a commercial image intensifier, which simultaneously converted it to a more-accessible visible region for detection by a standard camera. The region of the images extracted for further analysis was 420 × 420 pixels, centered approximately on the probe region.

The intensity of each pixel in the image was proportional to the number density of OH in the probed quantum state, modulated by well-known spectroscopic line strength factors,[84] and by spatial variations in the LIF detection efficiency. These variations result mainly from the distribution of power across the probe laser sheet in the z-direction, transverse to its propagation along x, in addition to aberrations and changes in collection efficiency in the imaging assembly that vary radially outward from the optical center of the image. There may be other local variations in the camera sensitivity, MCP gain, and transmission of the filter or other optical elements, but these are expected to be relatively minor. Regardless of their source, the combined variations constitute what we term the "instrument function" (IF). (Note that this is independent of the FB correction described above and affects all images independently of the dimensions of the molecular beam or θ_i.)

The primary IF correction (which we label IF1) was determined experimentally by creating a uniform OH number density across the probe region and measuring the resulting images. Details of the IF measurement procedure and how the results were used to correct the experimental scattering images are given in the supplementary material. For some of the measurements to follow, a minor secondary correction was derived, which made it possible to ensure self-consistency of the intensity of the propagating in-going OH packet, as also described in the supplementary material; we term this version IF2. The effects of the instrument function on the systematic reliability of measured angular distributions are discussed at relevant points below. In general, although, and as an objective in the future work, it would clearly be desirable for the IF to be as flat as possible across the observed region. This would minimize the extent of the correction required and reduce the scope for systematic errors.
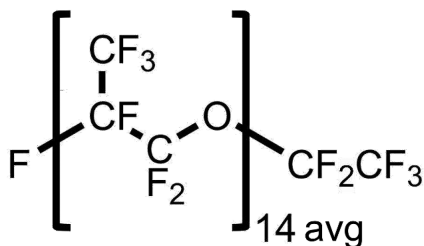

FIG. 2. Structure of a typical PFPE molecule. Krytox® 1506 contains a mixture of different chain lengths, with an average chain consisting of 14 monomers.

To allow for reliable measurements of distances and hence ultimately of absolute molecular speeds, the conversion factor between the pixel space in the images and real space in the chamber was measured by imaging a grided target illuminated *in situ* by the laser sheet. (See supplementary material for the description of this process.) This conversion factor was measured to be 0.2495 ± 0.0074 mm px^{-1}. This is also significantly more reliable than the less-directly estimated value of 0.17 mm px^{-1} in our previous work.[73]

Two types of experimental images were taken during data acquisition. The first, as in our previous work,[73] were "image sequences" that captured the entire time evolution of the scattering process. These are necessary for the extraction of scattered speeds, for which they were best adapted. Each image sequence consisted of 56 frames, taken between discharge-probe delays of 68 and 178 μs at 2 μs intervals. Each frame was a sum of 500 individual single-laser shot images. The earliest four frames preceded the front edge of the in-going OH packet reaching the probe region; they were averaged and subtracted from the other frames to eliminate background camera noise. Image sequences with the PFPE surface removed from the main chamber (so-called "surface-out" images, compared with the "surface-in" images with the PFPE present) were also recorded, as they were needed to eliminate the in-going OH beam signals in the analysis (see the "Results" section and supplementary material for further details). For scattered signals, OH N = 2, 3, and 4 were probed; the relatively high population in N = 1 in the in-going packet prevented its reliable subtraction; hence, systematic scattering data were not recorded for this level. For each probed rotational level, six independent sequences were taken and averaged to account for random variations. This process was repeated with the OH beam at both angles of incidence, $\theta_i = 0°$ and $\theta_i = 45°$.

Complementing the image sequences, the second type of measurement was a new approach, which we label "extended images." These were designed to optimize the information on angular distributions by summing a large number (50 000) of single-laser-shot images at a particular discharge-probe delay. They were taken only for $\theta_i = 45°$, for which the angular distributions are more insightful as explained below and for the same set of probed OH rotational levels. Two delays were chosen; 132 μs, corresponding to the peak signal of scattered OH, and 152 μs, which was later by approximately the temporal width of the in-going OH packet. The residual in-going OH beam signal and background camera noise were removed by subtracting extended "surface-out" images.

MOLECULAR DYNAMICS SIMULATION PROCEDURE

MD simulations were carried out using GROMACS (version 2020.2).[85,86] The PFPE molecules were modeled using the OPLS-AA force field,[87] with parameters specifically optimized recently for molecules of this type[88] being obtained from the Foyer program (version 0.11.3).[89] A cubic box of dimension 8.8 nm and periodically repeating boundaries was filled with 300 PFPE molecules having the chemical structure shown in Fig. 2; a monodisperse system with n = 14 was assumed for simplicity in the current illustrative work. The sample was energy-minimized and then equilibrated at 298 K before one dimension of the box (conventionally the z-axis in the MD literature—this also coincides with the lab-frame z-axis defined in Fig. 1) was expanded to 26.5 nm, creating equal volumes of

vacuum above and below the slab of PFPE. The slab was then NVT (constant number of molecules, volume, and temperature) equilibrated using the leapfrog algorithm and a 0.5 fs time step. The equilibration procedure used cycles of 20 ns NVT at 298 K followed by an annealing step of 0.5 ns at 400 K. A total of four cycles were used, with each 20 ns run being compared with the previous one to confirm equilibration. Only the final 10 ns of the final 298 K NVT run was used for analysis.

RESULTS

Representative examples of the experimental image sequences can be seen in Fig. 3 (Multimedia view) and Fig. 4 (Multimedia view) for OH in N = 3 scattered from PFPE with $\theta_i = 0°$ and $\theta_i = 45°$, respectively. These sequences are raw signals, directly as acquired without instrument-function or other corrections. In the multimedia view, the videos show the in-going OH packets crossing the probe region (at the relevant θ_i) followed by the scattered plumes at longer delays.

A selected representative frame from each of the sequences in Figs. 3 and 4, adjusted for the IF (as noted above and via the procedure explained in detail in the supplementary material; the IF2 version has been used here), is shown in Fig. 5. These images represent the best estimate of the true number-density distribution of OH (N = 3) in the xz-plane under these conditions with an incident beam of the specified characteristics. Only the parts of the images corresponding to the probe region are shown, defined by a drop in the IF to 20% of its peak values. This noise naturally increases toward the edges as the IF declines. The chosen delay of 132 μs corresponds approximately to the peak intensity of the scattered plume. A simple
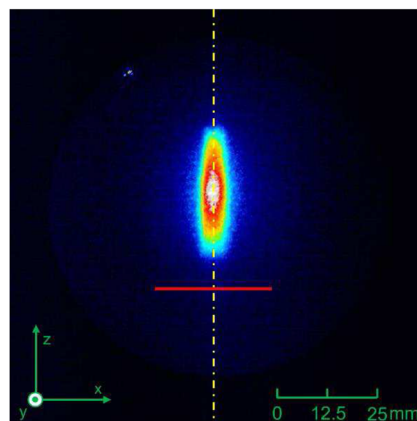

FIG. 3. A selected frame (discharge-probe delay of 94 μs) from a raw image sequence of OH (N = 3, $\theta_i = 0°$) scattering from the surface of PFPE. The image is false-colored, where black indicates pixel intensity of 0; white, the maximum intensity; and a spectrum of colors from blue to red indicate intermediate intensities. The red line indicates the position of the PFPE liquid surface; the wheel lay in the xy plane and rotated about the z-axis. The yellow-dashed line is the normal to the surface positioned at the point of impact of the transverse center of the in-going OH beam on the surface. Added in green are the coordinates of the experimental setup, as defined in Fig. 1, and an absolute distance scale. (The bright white spot in the top-left quadrant is a small region of damage on the detector.) (Multimedia available online).
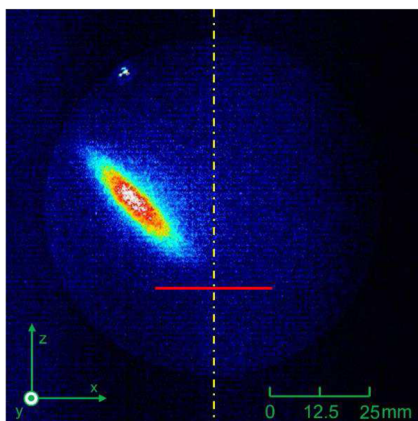
FIG. 4. A selected frame (discharge-probe delay of 94 μs) from a raw image sequence of OH ($N = 3$, $\theta_i = 45°$, in the xz plane) scattering from the surface of PFPE. All other features as in Fig. 3. (Multimedia available online)

visual comparison reveals fundamental differences in the scattered OH angular distributions for the different θ_i. For $\theta_i = 0°$, the scattered OH is concentrated in a relatively narrow plume, quite strongly focused back along the surface normal [see Fig. 5(a)]. In contrast, for $\theta_i = 45°$, the scattered plume is broader and, on careful inspection, asymmetric about the normal [Fig. 5(b)]. Related differences are also apparent in the raw image sequences in Figs. 3 and 4, and hence, the contrasts between incidence angles cannot be the result of application of the instrument function.

To facilitate the analysis of the time-varying OH spatial distribution, the images were divided into specific regions of interest
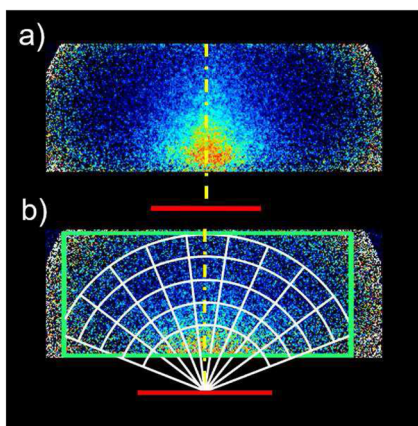

FIG. 5. Selected frames from the IF-adjusted image sequences (using IF2) of OH ($N = 3$) with (a) $\theta_i = 0°$ and (b) $\theta_i = 45°$ scattered from surface of PFPE and measured at the discharge-probe delay of 132 μs. The green rectangle superimposed on (b) indicates the analyzed region, bounded approximately to top and bottom by edges of the probe sheet. The series of white concentric arcs and radii stemming from the central point of impact (i.e., the intersection of the red line indicating the surface position and the yellow dashed line indicating the normal to the surface) in (b) define the ROIs used in the analysis of the image sequences.
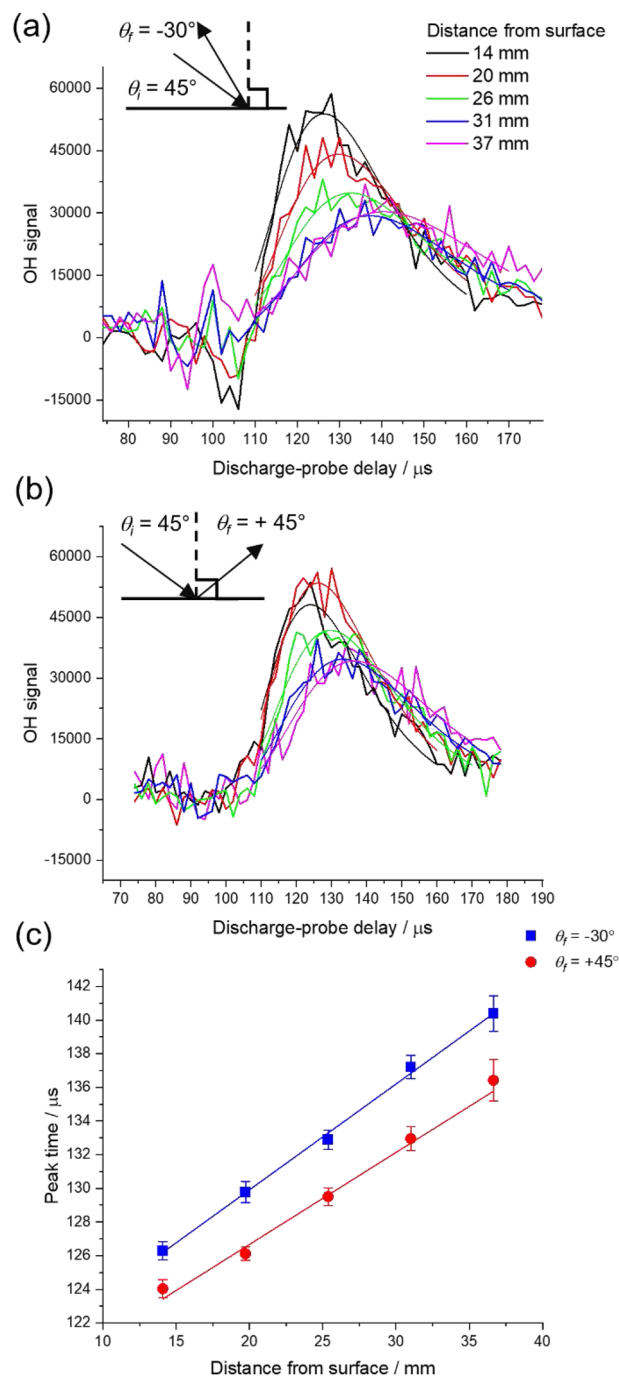

FIG. 6. Scattered OH ($N = 3$) ToF appearance profiles at $\theta_i = 45°$, with in-going signal subtracted, drawn from ROIs placed at consecutive radial distances from the PFPE surface along (a) $\theta_f = -30°$ or (b) $\theta_f = 45°$. The Gumbel distribution fits are also shown as smooth lines of corresponding colors. (c) Discharge-probe delays at the peaks of the ToF appearance profiles are plotted against the distance of the ROI to the surface for $\theta_f = -30°$ (blue squares) and $\theta_f = +45°$ (red circles). The error bars are 1σ standard errors in the peak delay coming from the fits in (a) and (b). Straight line fits (with unconstrained intercepts) are also shown in corresponding colors.

18 September 2023 03:06:04

(ROIs). A crucial aspect of any such an approach is to establish the correct origin. To achieve this, the probe laser sheet, normally displaced by ~10 mm along the z-direction, was moved as close as possible to the surface. Extended images were taken, which unambiguously identified the center of the point of impact of the in-going molecular beam on the PFPE surface. Further details are provided in the supplementary material.

In our previous proof-of-concept work,[73] we introduced the ROI concept using small, square regions. We have refined that in the current work to ROIs defined by arcs and radial straight lines, as shown in Fig. 5(b). The focus of the arcs coincided with the origin. This construction recognizes that scattering into a given angular range in the plane of the image will occupy a larger area as the molecules propagate radially outward. These types of ROIs, therefore, maximize the use of the data, without any loss of angular resolution as a function of radial distance. They compensate for the natural drop in intensity per unit area due to in-plane divergence (but not, of course, due to the separate effect of the out-of-plane scattering). ROIs were labeled according to the distance from their center point to the origin (14, 20, 26, 31, and 37 mm) and the angle at which they were centered (at this stage in the analysis, from −60° to +60° in 15° steps; by convention the negative scattering angles indicate positions to the incident side of the normal for $\theta_i = 45°$ - left, as viewed on images). Only the ROIs that lay fully within the probe region were considered in the further analysis.

For each image in a sequence, the intensities of pixels within each ROI were summed and plotted against the discharge-probe delay to produce ToF appearance profiles. These represent the time variation of pLIF signal, and by extension, the relative OH number density, within a particular probe volume defined by the area of the ROI and the thickness of the laser sheet. Examples can be seen in Fig. 6 for OH in $N = 3$ with $\theta_i = 45°$, where the profiles at differ-ent distances centered on $\theta_f = −30°$ are compared with those along $\theta_f = 45°$. The contribution from the in-going OH beam has been removed by subtracting the corresponding profiles with no PFPE surface present (see Sec. S5 of the supplementary material). Because the "surface-in" and "surface-out" sequences were taken independently, random differences resulted in imperfectly subtracted residual signals preceding the onset of the scattered signal at around 110 μs. This noise is naturally generally worse in directions closer to the in-going beam.

The metric that we concentrate on here is the most-probable speed of the scattered wave of OH. To determine it, the region of the ToF profile in the vicinity of its peak (delays between 110 and 160–170 μs, depending on a particular profile) was fitted to an arbitrary function (Gumbel distribution function) of appropriate shape:

$$I(t) = A \exp\left[1 - \exp\left[-\left(\frac{t - t_c}{w}\right)\right] - \left(\frac{t - t_c}{w}\right)\right], \quad (1)$$

where $I(t)$ is the summed intensity in the ROI, A is the peak amplitude, w is a width parameter, t is the discharge-probe delay, and t_c is the best-fit delay of interest, corresponding to the peak of the distribution. There is generally, as expected, a clear shift of the peaks to later delays with increasing distance from the surface along a single θ_f. These show a linear relationship, as can be seen in Fig. 6(c). The inverse slopes give the corresponding most-probable scattered OH speeds. The intercept represents the nominal time of arrival of the peak of the incident packet at the surface. In practice, there is a slight dependence on the scattering angle—this is a reproducible geometric effect whose source is identified in Paper II.[81]

The dependences of the most-probable speeds on θ_f for each θ_i and the different OH rotational levels are shown in Fig. 7. The most-probable speed in a thermal sample (540 m s^{-1}) at the temperature

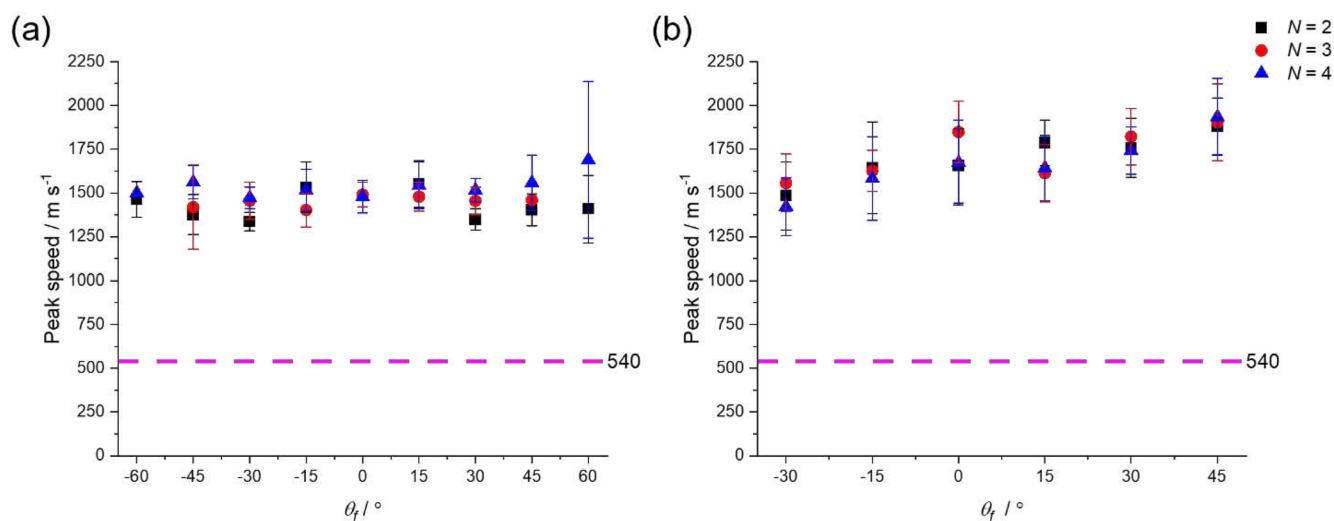**FIG. 7.** θ_f-dependent most-probable scattered speeds for (a) $\theta_i = 0°$ and (b) $\theta_i = 45°$ for OH in $N = 2$ (black squares), 3 (red circles), and 4 (blue triangles). The error bars (1σ) come from the uncertainties in the slopes of the straight-line fits of peak delay vs distance [see Fig. 6(c)]. Points where the straight-line fits were poor and generated large error bars, particularly where the final angle was coincident with the in-going beam, have been omitted. Also shown (magenta dashed line) is the most probable thermal speed (~540 m s^{-1}) of OH at 298 K.
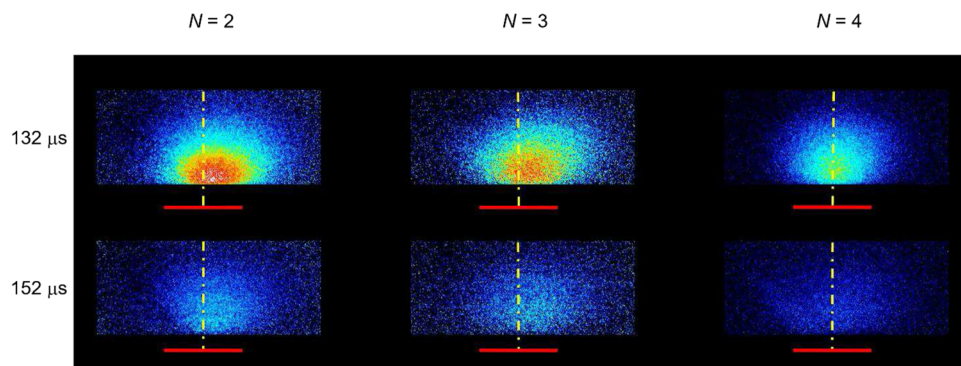
FIG. 8. Extended images of PFPE-scattered OH ($\theta_i = 45°$) taken at two discharge-probe delays: 132 μs (top row) and 152 μs (bottom row). The images were cropped to show only the probe region as defined by the ROI analysis [see Fig. 5(b)]. The red lines indicate the position of the PFPE surface (~10 mm away from the closest edge of the probe region) and the yellow dashed lines the normal to the surface positioned at the point of impact of the transverse center of the in-going OH beam on the liquid surface (established independently as described in the text). Some images ($N = 3$, 132 μs and $N = 4$, 152 μs) show weak residual signals in the in-going beam direction due to imperfect subtraction.

of the liquid (298 K) is also shown for comparison. The full sets of speeds are also tabulated in the supplementary material. These measurements corroborate the principal results in our previous study; all the absolute speeds are somewhat higher here as a result of the distance-conversion-factor recalibration, but the trends and qualitative conclusions are not materially altered.[73] The most-probable scattered OH speeds are very obviously universally superthermal, regardless of any of the experimental parameters (N, θ_i, and θ_f). Overall, the average most-probable speeds, weighted across the angular distributions and by the populations of rotational levels, were found to be 1470 m s^{-1} for $\theta_i = 0°$ and 1590 m s^{-1} for $\theta_i = 45°$. For $\theta_i = 0°$, there is no clear trend with θ_f; in our previous work, a subtle increase in speed with larger θ_f was discernible.[73] The signal-to-noise for this particular measurement was higher in the previous work because of the less-apertured beam. We have assessed through the modeling in Paper II[81] whether the broader beam profile there would have distorted the apparent speeds significantly. We conclude from this that the trends with θ_f are still reliable, if not their absolute values. For $\theta_i = 45°$, there is a clear trend here of increasing speed with increasing θ_f, as was also observed previously.[73] There is little systematic variation with the OH rotational level.

As noted above, the image sequences are optimized to determine the information on scattered speeds. The angular distributions are better quantified via the extended images recorded at fixed delays. They were measured only for $\theta_i = 45°$, for which the results are more diagnostic of the scattering mechanism (see below). A substantial change in the range of speeds predominantly being sampled was achieved by selecting delays of either 132 μs, corresponding to the peak of the scattered wave being in the central regions of the image, or 152 μs, when the tail of the distribution dominates. Figure 8 shows these images for the three different rotational levels. As described in the "Experimental" section, contributions from the in-going beam and other background signals have been removed by subtracting the corresponding surface-out images. Imperfections in the subtraction leave small residual signals and generally poorer signal-to-noise in the direction of the in-going beam.

The left–right asymmetry of the scattered plumes is clearly visible in these images, with dominant scattering to the specular side. The angular distributions were quantified using a similar ROI method to that applied to the image sequences. The arc distances remained the same, but the angular resolution was increased by reducing the spacing to 7.5° (resulting in a new set of θ_f values from
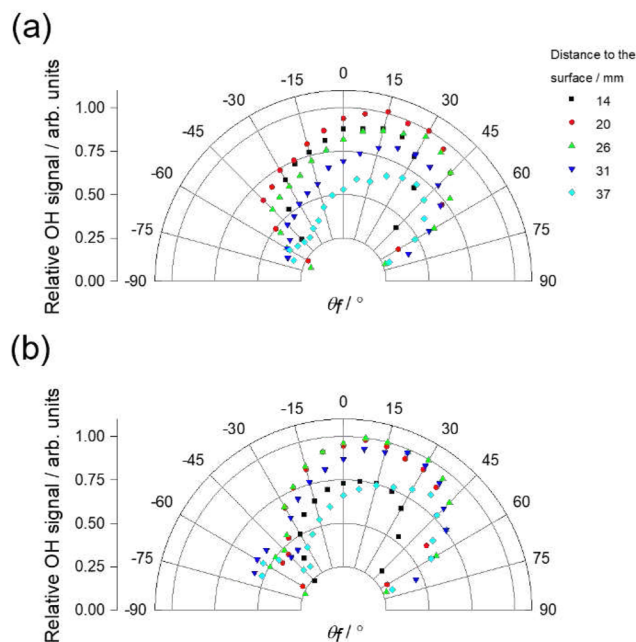

FIG. 9. The distance-dependent scattered OH ($N = 2$, $\theta_i = 45°$) angular distributions measured as summed spatially resolved pixel intensities from extended images taken at discharge-probe delays (a) 132 μs and (b) 152 μs. Some residual in-going OH beam signal can be seen along $\theta_f \approx -60°$, particularly in (b).

$-67.5°$ to $+67.5°$ in $7.5°$ steps). The summed intensity in each ROI was obtained as a function of θ_f for each radial distance from the surface.

Figure 9 shows the angular distributions at different radial distances for OH $N = 2$ extracted from the extended images at the respective discharge-probe delays. All the distributions show a very distinct tendency toward scattering on the specular side but peaking at sub-specular θ_f. Moreover, the distributions at the later delay of 152 μs show OH scattering with θ_f closer, on average, to the surface normal, albeit still not directed along it. This indicates that the dominant θ_f is speed-dependent, with slower molecules (i.e., those still present in the image at 152 μs vs those at 132 μs) tending toward less specular scattering. This gross difference between delays is a secure conclusion, but it may also be reflected within the image at either delay, with those in arcs closer to the surface having the least specular distributions. Some care is needed not to overinterpret these subtler effects, however, because the instrument function varies most rapidly at the largest distances from the surface and hence is most susceptible to introducing systematic distortions there. There is also an additional purely geometric effect due to finite size of the incident beam that can produce the same appearance of broadening of the angular distribution closer to the surface. This has been quantified through the simulations in Paper II,[81] which show that these purely geometric effects differ by less than the typical experimental uncertainties for the three innermost arcs of ROIs. Consequently, their results were averaged here to enhance the signal-to-noise when assessing the N-dependence of the angular distributions.

These averaged distributions are compared for OH in $N = 2$, 3, and 4 in Fig. 10 for both discharge-probe delays. The left panels [(a)(i) and (b)(i)] show the distributions extracted from the raw images. The right panels (a)(ii) and (b)(ii) are the results of applying both the instrument-function (IF) and finite-beam (FB) corrections (as introduced above and derived in detail in Paper II[81]) and hence show our final, best estimates of the true angular scattering distributions. The IF1 versions of the instrument function (i.e., those that were measured directly in tandem with the $\theta_i = 45°$ extended images) were used here because the IF2 secondary correction was not possible without extended images for $\theta_i = 0°$. Any systematic differences in the angular distribution resulting from the choice of IF are, however, relatively minor. The effects of applying IF1 alone are shown in the supplementary material. They display the expected enhancement of signals at wider scattering angles, where the average detection sensitivity is lower. Fortuitously, the FB correction acts in the opposite sense because measured signals at wider angles are artificially enhanced due to the lateral spread in the in-going beam. Consequently, the combined effect of both corrections to the raw distributions is relatively modest, as can be seen by comparing the left- and right-hand panels in Fig. 10.

Notably, qualitative trends that are apparent in the raw angular distributions survive in the corrected versions. Interestingly, at the earlier delay, scattered OH in $N = 2$ and 3 show very similar angular distributions, whereas $N = 4$ shows a noticeable shift toward less specular angles. At the later delay, the distributions are less specular for all three rotational levels, which are now very similar to each other.
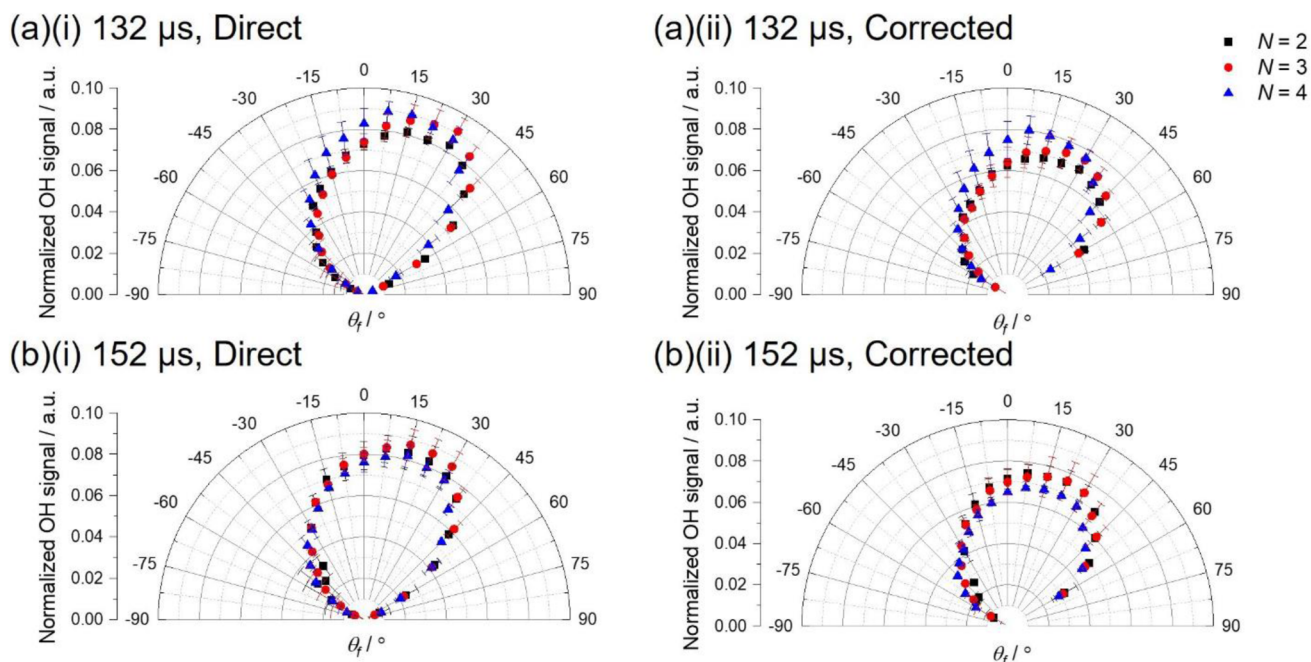
FIG. 10. The rotational-level-dependent scattered OH angular distributions for $\theta_i = 45°$, averaged over the three inner arcs of ROIs (distances to surface of 20, 26, and 31 mm) from extended images taken at discharge-probe delays of (a) 132 μs and (b) 152 μs. In each case, (i) they are measured directly from the images, (ii) following both the instrument function (IF1) and finite-beam (FB) corrections.
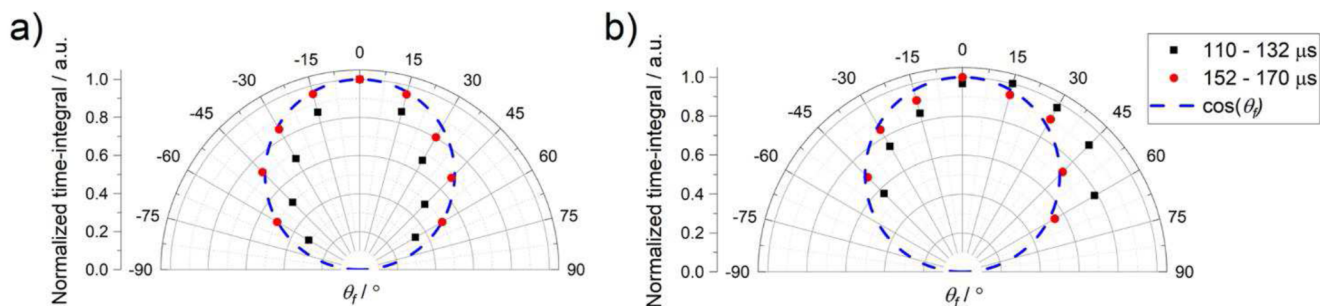
FIG. 11. Scattered OH angular distributions for OH ($N = 3$) (a): $\theta_i = 0°$, and (b) $\theta_i = 45°$ measured as θ_f-dependent time-integrals in delay ranges of 110–132 μs and 152–172 μs, as indicated. Radial distance from the surface = 26 mm. A $\cos(\theta_f)$ distribution is shown for comparison.

Some corroboration of the main results from the extended images can be derived from the image sequences; although they were not optimally designed for this purpose, it is possible to extract angular distributions from them. In principle, scattering-angle distributions would ideally be expressed as a flux of molecules into a given angular range. This is not possible, however, without knowing the full distribution of scattered speeds as well as accounting for the spread in arrival times at the surface. We have shown in Paper II,[81] although, that the results of summing the ToF profiles between reasonable time limits for a given ROI are only marginally different from the input angular distributions assumed in forward simulations. The time-sum was determined as a function of θ_f for each rotational level. Two distinct sets of limits were chosen to assess whether there is any correlation between the angular distribution and scattered speed. The first region spanned discharge-probe delays from 110 to 132 μs, corresponding to the fastest scattered OH molecules up to roughly those with the most-probable speed. The second covered the tail of the ToF profiles, from 152 μs onward; this should encompass any OH with the most-probable thermal speed, as demonstrated in Paper II[81] and discussed further below.

Representative polar plots of these time-sums for OH $N = 3$ at radial distance of 26 mm are shown in Fig. 11. The results for other distances were similar, consistent with the results in Paper II,[81] which show that geometric effects vary little with distance for either incidence angle; these FB corrections have been applied to the data in Fig. 11. The corresponding measured angular distributions for $N = 2$ and 4 were similar, as shown in the supplementary material. Overall, they confirm the obvious differences between $\theta_i = 0°$ and 45° that can be seen by eye in the raw image sequences. For $\theta_i = 0°$, the distributions are left–right symmetric and quite sharply directed along the normal at early delays, broadening at later delays. For $\theta_i = 45°$, the results also corroborate the main features of the extended images, with considerable asymmetry toward the specular side at early delays, which becomes less pronounced at later delays.

DISCUSSION

The principal new results in this work are the angular distributions of OH scattered from PFPE at $E_i \approx 35$ kJ mol^{-1}. Improvements in angular resolution have allowed them to be observed reliably for the first time here. The bulk of the scattering for $\theta_i = 0°$ is found to be quite sharply directed back along the normal. At $\theta_i = 45°$, the distribution is somewhat broader and distinctly asymmetric, with the dominant θ_f toward the specular side but peaking in a sub-specular direction. For both incidence angles, the angular distributions are correlated with scattered speed, broadening at lower speeds and, for $\theta_i = 45°$, becoming less specular.

These new observations reinforce and substantially extend our conclusion from previous distinct measurements that at this collision energy, the bulk of the scattering is much closer to the IS than the TD limit. The superthermal peak speeds and their correlations with θ_i and θ_f, observed previously, but confirmed here, support this conclusion.[73] It is further reinforced by previous measurements (confirmed qualitatively by relative OH signal sizes observed here) of non-thermal rotational distributions, characteristic of the ballistic translational-to-rotational energy transfer.[38–40,47]

As noted in the Introduction, the separation into IS and TD, although empirically useful, is ultimately artificial and not sustained at molecular level in realistic scattering calculations.[7,30,32–36] We can assess if there is anything independent in our measurements here that implies the need to invoke any fully TD behavior.

The original way to discriminate TD from IS was on the basis of scattered speeds, as in previous work based on MS detection where the TD component was extracted by fitting a Maxwell–Boltzmann distribution to the low-energy tail of the scattered ToF distribution;[48,50,51,90] the IS component was then obtained by subtraction. In a similar spirit, we have forward-simulated the ToF distributions that would have been observed for OH molecules scattered with a TD speed distribution at the liquid temperature, using the methods described in detail in Paper II[81] to account for all the experimental geometric factors and spread of arrival times of the incident molecular beam packet. A representative example is shown in Fig. 12 (black line), compared with the data from Fig. 6(b) for $\theta_f = \theta_i = 45°$ and an arc distance of 31 mm. This shows clearly that a large majority of the scattered molecules have superthermal speeds. We can safely conclude that any TD component is at most a minor contribution, with an upper limit of around ~20% based on matching by-eye of the intensity of the tail at the longest delays. Qualitatively similar results are found for other combinations of angles and probed rotational levels.
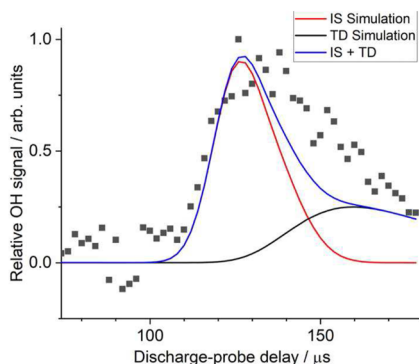
FIG. 12. ToF profiles for $\theta_i = 45°$ and $\theta_f = +45°$ (i.e., specular scattering). Experimental data for OH ($N = 3$) (black squares). Simulated profiles assume either a TD distribution (black line) or soft-sphere impulsive model (red line) of scattered speeds. The blue line is the sum of the IS and TD simulations, showing that this does not adequately describe the experimental data.

An alternative approach is to forward-predict an IS-like distribution according to an assumed model; we have done this using the established "soft-sphere" model in Paper II.[26–28] The results are also illustrated in Fig. 12. The model reproduces the most-probable speed by construction, through the selection of the values of the adjustable parameters. The finite width of the simulated *scattered* profile results from the input spread of *incident* speeds and other geometric factors, designed to reproduce the independent measurements on the incident beam. The IS simulated profile is clearly narrower than the experimental scattered profile. This leads to the important conclusion that the experimentally observed spread in scattered speeds is a feature of the scattering dynamics and not simply limited by the experimental speed resolution. In physical terms, this implies that the single-valued relationship between speed and scattering angle that is inherent in the soft-sphere model is not a good description of OH scattering at the PFPE surface.

No weighted sum of the soft-sphere-model IS and TD contributions will recover the observed ToF profile, as also illustrated in Fig. 12 (blue line). Scattering at a given angle must, therefore, result in quite a broad distribution of speeds that extends to lower values than predicted by the soft-sphere model and into the region significantly populated in a thermal sample. This ultimately reflects the nature of the interaction with liquid surface, to which we return below having also considered the angular distributions. However, we note that there is no obvious bimodality in the speed distributions of the type seen in some other experiments where the IS/TD separation has been implemented.[27,28,48] It is, therefore, not clear that carrying out a subtraction of a TD component here to recover a "pure IS" distribution, independent of any model assumptions, is objectively justified or would provide any additional physical insights.

Turning to angular distributions, we have, in effect, isolated molecules that have speeds compatible with being part of a TD component on the basis of discharge-probe delay; in the extended image measurements, the later delay of 152 μs (see Fig. 8 and following figures) was chosen to fall into the "TD" region, as does the 152–172 μs window (Fig. 11) for the time-sum analysis of the image sequences. It is certainly true for $\theta_i = 0°$ that the time-sum distribu-

tion, which is always observed to be left–right symmetric as expected by symmetry, broadens at the later delay and resembles more closely the $\cos(\theta_f)$ distribution that would be expected for TD. However, for $\theta_i = 45°$, there is still some distinct left–right asymmetry in the distributions for the later delays in both the time-sum measurements (Fig. 11) and more clearly in the better-determined extended images [Fig. 10(b)]. Hence, even at these later delays, the angular distributions have not reached the full TD limit.

Bimodality in the observed rotational-state-population distributions has also been used to infer the presence of a TD component in previous inelastic scattering studies.[62,91] In the current work, the sparsity of the populated OH rotational levels precludes any such analysis. Nevertheless, if there were a significant TD component, we would expect this to be apparent in the variation of the angular distribution as a function of rotational state. A 300 K rotational distribution peaks in the lowest levels, with almost equal populations in $N = 1$ and 2. We were not able to measure $N = 1$ angular distributions for reasons explained above but can compare the results for $N = 2$, which might be expected on this basis to have a larger contribution from TD and, therefore, be more $\cos(\theta_f)$-like than those for $N = 3$ and especially $N = 4$. Interestingly, this is not what is observed here. $N = 2$ and 3 show similar distributions, but $N = 4$ is systematically broader and slightly more sub-specular (i.e., *more* back-scattered toward the normal). We come back to potential dynamical explanations below, but these trends are certainly not those expected for TD behavior.

Overall, we can conclude that any TD contribution at these collision energies is at most minor. There is nothing objective in our data that indicates a binary separation between it and the majority IS component, nor anything that cannot be explained by a progressive broadening of the angular distributions for slower scattered products.

Returning to the dominant IS component, what do the measurements reveal about the scattering mechanism and about the characteristics of the PFPE liquid surface? Note again that all the distributions for $\theta_i = 45°$ peak in sub-specular directions. This is not what would be predicted by the simple hard-cube models mentioned in the Introduction.[6,23–26] The transfer of some fraction of the normal component of the momentum to recoil of a locally flat and initially static surface "particle" with a finite mass, with retention of the parallel component, will always give *super*-specular (i.e., shifted from specular toward more-grazing angles) scattering. Neglecting a significant contribution from thermal motion of the surface, which we expect to be a good approximation here because of the relative masses involved and the ambient temperature of the liquid, sub-specular scattering, combined with relatively broad angular distributions, requires a non-microscopically flat surface. This conclusion has been reached from previous scattering studies of, e.g., noble gases from PFPE and other long-chain liquids such as squalane by Nathanson, Minton, and co-workers.[49–51] It is consistent, in particular, with the observed systematic broadening of the angular distributions with increasing liquid temperature, inferred to be the result of increased thermal roughening.[51] The new results here imply that OH also senses a microscopically rough PFPE surface at room temperature.

Interestingly, although the structure of the PFPE surface has been inferred from secondary-ion mass spectrometry (SIMS) and angle-resolved photoelectron spectroscopy (ARXPS) to be
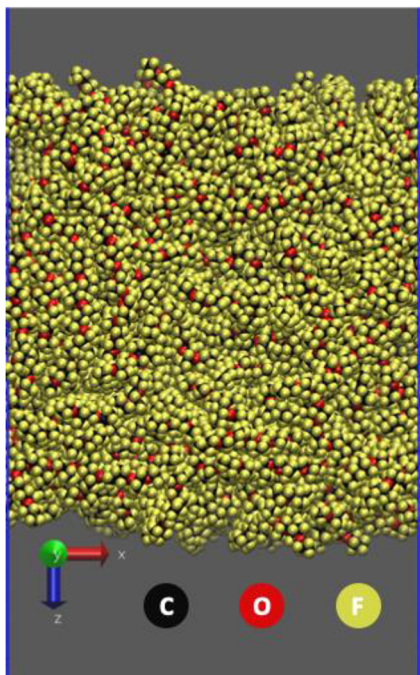
FIG. 13. Representative snapshot (side view) from an MD simulation of a slab of liquid PFPE (300 molecules of monodisperse F-[CF(CF$_3$)CF$_2$O]$_{14}$–CF$_2$CF$_3$). The sample has been thermally equilibrated at 298 K. Periodically repeating boundary conditions (x × y dimensions = 8.8 × 8.8 nm^2, with vacuum above and below the slab, along z). Whole molecules that project partly through the boundary of the box in the direction of view (along y) are not truncated. Atom types are color-coded as indicated.
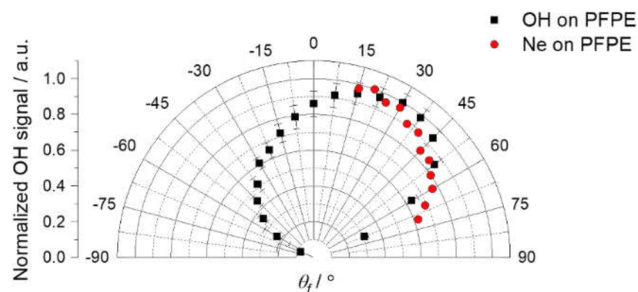

FIG. 14. Comparison between the rotational-level-population-weighted average angular distribution of the OH scattered from a PFPE surface measured at the discharge-probe delay of 132 μs in this work with the angular distribution of the IS component of Ne scattered from a PFPE surface measured using mass spectrometry by King et al.[49] The collision energies were similar: 35 kJ mol^{-1} here for OH, and 29 kJ mol^{-1} for Ne. θ_i = 45°.

dominated by CF$_3$ groups, with little exposure of the O-containing components of the chain,[36,91–93] this picture of the surface has never been supported independently by computation. In the original work of Nathanson and co-workers, the likely nature of the PFPE surface was argued by analogy with early simulations of long-chain n-alkanes.[50] We have carried out some preliminary MD simulations to establish the basic features, using a forcefield recently developed specifically for PFPEs.[88] A representative snapshot is shown in Fig. 13. This demonstrates that the surface (i.e., upper and lower faces of the slab) is indeed microscopically rough, with a significant number of chain-ends and folded segments projecting above the average plane of the surface, interspersed by crevices and depressions. (A fuller, systematic MD study characterizing of the PFPE surface is currently under way.[94])

At least at a qualitative level, therefore, the MD simulations strongly support the conclusions based on the interpretation of angular distributions; this surface topology would very likely result in OH being scattered into a wide range of final angles even in single-collision events. Given the kinematics, these effects of surface roughness are enhanced for lighter projectiles. In previous work, angular distributions were found to be notably broader and more sub-specular for Ne (mass 20 amu), which is kinematically most similar to OH (mass 17 amu), than for the heavier noble gases.[49] We have compared in Fig. 14 the shape of the angular distributions for OH scattering at the peak of the speed distribution here with the IS

component of Ne scattering for the same θ_i = 45° and at a similar collision energy reported by Nathanson, Minton, and co-workers.[49] The OH results are an average over the observed rotational levels, N, weighted by their known relative populations. (As noted, we do not have measurements for N = 1, but we do not expect its omission to have a large effect on the overall OH distribution.) In the regions where both approaches were able to make measurements, the OH and Ne results are strikingly similar. We note again in passing that this highlights the capability of the current pLIF method to measure a wider range of angles than a rotatable MS-detector in combination with a molecular beam source. We might also reflect that neither distribution conforms to the popular preconception of being strongly directed along the specular direction, despite having dominant IS character.

This similarity with Ne suggests that the scattering of OH from PFPE is not strongly perturbed by it being a linear rotor. This is perhaps not too surprising, given the limited fraction of the initial kinetic energy transferred to rotation. The highest observed rotational level here (N = 4) corresponds to only 12% of E_i. The previously measured rotational distributions fit reasonably well to a rotational temperature of 400 K,[47] which is equivalent to only 9% of E_i appearing on average in rotation.

Similarly, although the scattered speeds we observe are somewhat θ_i- and θ_f-dependent (see Fig. 7), for θ_i = 0°, the average most-probable speed across all θ_f, weighted by the rotational populations is as noted above, around 1470 ms^{-1}, or a kinetic energy of 18.4 kJ mol^{-1}. This is 52% of the initial kinetic energy, so the average fraction of the energy lost from translation is 48%. This implies that most of this must be lost either to collective recoil or other motions of the surface, as described by the surface mass and E_i parameters of soft-sphere models, respectively,[27–29] significantly outweighing the relatively modest amounts transferred to OH rotation.

We now compare our results with the prior QCT calculations of OH scattering from a model F-SAM surface at somewhat higher collision energy (E_i = 54 kJ mol^{-1}).[37] As Troya noted, the predicted rotational distributions agreed well with those observed in our own earlier photolytically generated OH experiments, which they were designed to simulate.[38,39] For the assumed θ_i = 0°, Troya's predicted average final translational energies were of order 4-5 times higher than his predicted rotational energies. They correspond to

around 65% of the initial energy being lost from translation. We had not measured translational energies in our earlier work, but can now reflect that this is, therefore, somewhat greater than 48% loss of energy from translation we deduce from the most-probable speeds here. However, note again the differences in E_i. Nathanson and co-workers' earlier MS measurements of the IS component of Ne scattering from PFPE show that only around 25% of the kinetic energy is lost at $E_i = 28$ kJ mol^{-1}, rising to nearer 40% at $E_i = 56$ kJ mol^{-1}.[50] This suggests that the fractional loss would also probably be larger for OH at higher E_i; hence, although no direct comparison is available under equivalent conditions, the QCT predictions for loss of translation from OH are broadly in agreement with our experiments here. The absolute comparison between the previous MS and current pLIF experiments implies quite clearly that more energy is lost from translational energy for OH than from Ne at similar E_i, and by somewhat more than can be accounted for simply by the additional loss to rotation. This discrepancy is interesting and remains to be explored further.

At the time of Troya's QCT calculations, there were no experimental results on angular distributions with which to compare. He noted that for $\theta_i = 0°$ at $E_i = 56$ kJ mol^{-1}, the predicted distributions were largely uncorrelated with *initial* rotational state; data resolved by final state were not reported.[37] The results were presented in a slightly different form, being integrated over all azimuthal angles rather than confined to a single plane as observed experimentally here. However, this can be accounted for (to a good approximation) by applying the relevant $\sin(\theta_f)$ factor to our current data for $\theta_i = 0°$ for, e.g., $N = 3$ from Fig. 11(a) and to the corresponding data for the other levels (given in the supplementary material). For the earliest time interval containing the most-impulsive scattering, the $\sin(\theta_f)$-weighted distributions here have broad peaks between 30° and 60°. They are qualitatively similar to those from the QCT calculations but peak on average at slightly wider angles, clustered around 45°, than the 30°–45° reported by Troya. These differences are subtle, but they would be consistent with the real PFPE liquid surface being somewhat rougher than the proxy F-SAM surface used in the QCT calculations.

Troya also predicted correctly, at least qualitatively, the correlation between scattered OH speed (or translation energy) and θ_f seen in Fig. 7 for $\theta_i = 45°$ and also discernible in our previous measurements with higher signal-to-noise for $\theta_i = 0°$.[73] As noted, this is a core feature of IS-like scattering where less momentum is transferred to the surface for smaller deflections. It is a natural prediction of hard and soft-sphere models and is generally supported by realistic scattering calculations on other systems.[37,73,95,96]

Finally, we return to possible dynamical explanations for the subtle but systematic variations in angular distributions for different N. We note in passing that it may well be possible to characterize these differences empirically by fitting them to a linear combination of one observed distribution and an adjustable amount of a $\cos(\theta_f)$ distribution, as suggested to be a "universal" characteristic of such angular distributions by Smoll and Minton.[36] (In our case, the base distribution would be for $N = 3$, being marginally the most specular.) We have not attempted that here because it was not clear what additional physical insights might be gained from the fitted parameters.

One possible physical explanation for the clear observation that $N = 4$ has the broadest and most back-scattered distribution is

that this could result from an increasing *number* of angular deflections, in each of which there is on average, an increase in rotational energy. A multi-deflection model of this kind, focusing on the complementary loss of initial translational energy, has been invoked previously by Nathanson and co-workers to explain the low-energy component of the translational distribution from scattering of noble gases at liquid-metal surfaces. It seems obvious from elementary considerations that multiple deflections will be probable at molecularly rough surfaces. For gas-phase scattering of a projectile atom or small molecule with an isolated target of approximately the size of the dangling groups that project above the surface of a liquid such as PFPE, it is very well known that the elastic scattering cross section would dominate the total scattering cross section. Even for the smaller fraction of collisions that are rotationally inelastic, those with small ΔN will tend to be strongly *forward* scattered.[97] This implies that the first interaction as the projectile approaches the liquid surface is likely to lead to a small deflection but not reverse the direction of the momentum along the normal. Such a reversal requires a so-called inner-turning-point (ITP) collision (in the language of Hase and co-workers).[33] The necessary lower-impact-parameter encounters become more likely as the projectile penetrates to higher-density regions of the liquid surface. Once the momentum is reversed, the recoiling projectile is also likely to suffer secondary, non-reversing deflections, further broadening the angular distribution. In Troya's QCT calculations on OH scattering from fluorinated SAMs, it was shown that single ITP events dominated (~90% of trajectories had only one ITP).[37] However, neither Troya, nor anyone else to our knowledge for related systems, has tried to quantify the number of weaker deflections that do not constitute ITPs and establish whether the final deflection angle or rotational state might be correlated with them.

An alternative explanation for the observed N-dependence of the angular distribution might be the character of the principal ITP collision, rather than the number of secondary, non-ITP deflections. As is also well known from gas-phase inelastic scattering of small molecules, the largest ΔN collisions require the lowest impact parameters, resulting in the most-backward scattering.[97] This is indeed consistent with what we see here for the highest observed level, $N = 4$. If correct, this represents a new, distinct dynamical effect which has not, to our knowledge, been noted previously in the context of *gas-liquid* (nor *gas-solid*) scattering.

It is not possible from qualitative arguments alone to disentangle which, if either, of these mechanistic possibilities is predominantly responsible for the observations here. However, they might hopefully help to inspire further experiments and future, more-detailed dynamical scattering calculations. In particular, the work of Troya on OH scattering from F-SAMs could be extended, both in terms of the trajectory analysis and perhaps incorporating a realistic MD description of the PFPE surface.[37] This might allow this, and related questions, to be answered and a deeper understanding to be gained of the subtleties of collisions of realistic liquid surfaces that go beyond the simple IS and TD paradigms.

CONCLUSION

Angle-resolved scattering of OH from liquid PFPE has been observed for the first time. At a collision energy $E_i = \sim35$ kJ mol^{-1}, impulsive scattering dominates; the majority of the scattered

molecules have superthermal speeds and their angular distributions depend markedly on incident angle. For $\theta_i = 0°$, the angular distribution is more concentrated along the normal than a $\cos(\theta_f)$ distribution, which is approached only for a minority component with the slowest speeds. For non-normal impact at $\theta_i = 45°$, the angular distributions are quite broad but clearly asymmetric toward the specular side and peak in a subspecular direction. They shift toward the normal for the minority slower products but do not reach a full a $\cos(\theta_f)$ distribution. The angular distributions are broadly similar to those measured previously for Ne scattering from PFPE at similar energies.[49] They reinforce the point that sharply directed, near-specular distributions are not the norm for relatively light projectiles scattering from molecularly rough surfaces. There are subtle but unexpected correlations between the angular distribution and OH rotational level, for which we identify at least two alternative potential dynamical explanations. The results here are in good general agreement, where the analyses overlap, with prior QCT predictions for OH scattering from a closely related model F-SAM surface at somewhat higher energy.[37]

SUPPLEMENTARY MATERIAL

See the supplementary material for the most probable speed of the incident OH packet; rotational population distribution in the incident OH packet; measurement and application of the instrument-function correction; calibration of the absolute distance scale in the experimental images; subtraction of the incident beam signal from OH ToF appearance profiles; identification of the central point of impact of the incident molecular beam; scattered OH most-probable speeds; effects of applying the instrument function alone to the observed angular distributions; time-integral angular distributions for all observed OH levels.

ACKNOWLEDGMENTS

AUTHOR DECLARATIONS

Conflict of Interest

The authors have no conflicts to disclose.

Author Contributions

All authors contributed to either the concept, design, execution, or interpretation of the research reported.

Maksymilian J. Roman: Investigation (lead); Methodology (equal); Validation (equal); Visualization (equal); Writing – original draft (equal); Writing – review & editing (equal). **Adam G. Knight**: Investigation (equal); Methodology (equal); Validation (equal); Visualization (equal); Writing – original draft (supporting); Writing – review & editing (equal). **Daniel R. Moon**: Investigation (supporting); Methodology (supporting); Validation (equal); Visualization (equal); Writing – original draft (supporting); Writing – review & editing (equal). **Paul D. Lane**: Investigation (supporting); Methodology (supporting); Validation (equal); Writing – original draft (supporting); Writing – review & editing (equal). **Stuart J. Greaves**: Investigation (supporting); Methodology (equal); Writing – original draft (supporting); Writing – review & editing (equal). **Matthew L. Costen**: Conceptualization (equal); Funding acquisition (equal); Investigation (equal); Methodology (equal); Supervision (equal); Validation (equal); Visualization (equal); Writing – original draft (equal); Writing – review & editing (equal). **Kenneth G. McKendrick**: Conceptualization (lead); Methodology (equal); Project administration (lead); Supervision (lead); Validation (equal); Writing – original draft (lead); Writing – review & editing (lead).

DATA AVAILABILITY

The data that support the findings of this study are available within the article and its supplementary material.

REFERENCES

[1] S. Decesari, M. C. Facchini, M. Mircea, F. Cavalli, and S. Fuzzi, J. Geophys. Res.: Atmos. **108**, 4685 (2003).

[2] X. Bai, N. Song, L. Wen, X. Huang, J. Zhang, Y. Zhang, and Y. Zhao, Green Chem. **22**, 895 (2020).

[3] B. Olmeda, L. Villén, A. Cruz, G. Orellana, and J. Perez-Gil, Biochim. Biophys. Acta, Biomembr. **1798**, 1281 (2010).

[4] M. Ramdin, T. W. de Loos, and T. J. H. Vlugt, Ind. Eng. Chem. Res. **51**, 8149 (2012).

[5] C. Wang, X. Luo, X. Zhu, G. Cui, D. E. Jiang, D. Deng, H. Li, and S. Dai, RSC Adv. **3**, 15518 (2013).

[6] G. M. Nathanson, Annu. Rev. Phys. Chem. **55**, 231 (2004).

[7] M. A. Tesa-Serrate, E. J. Smoll, T. K. Minton, and K. G. McKendrick, Annu. Rev. Phys. Chem. **67**, 515 (2016).

[8] A. T. Lambe, T. B. Onasch, P. Massoli, D. R. Croasdale, J. P. Wright, A. T. Ahern, L. R. Williams, D. R. Worsnop, W. H. Brune, and P. Davidovits, Atmos. Chem. Phys. **11**, 8913 (2011).

[9] N. M. Donahue, A. L. Robinson, E. R. Trump, I. Riipinen, and J. H. Kroll, in Atmospheric and Aerosol Chemistry, Topics in Current Chemistry Vol. 339, edited by V. McNeill and P. Ariya (Springer, Berlin, Heidelberg, 2012), pp. 97–143.

[10] S. Enami and A. J. Colussi, Mass Spectrom. **7**, 1 (2018).

[11] H. Tong, A. M. Arangio, P. S. J. Lakey, T. Berkemeier, F. Liu, C. J. Kampf, W. H. Brune, U. Pöschl, and M. Shiraiwa, Atmos. Chem. Phys. **16**, 1761 (2016).

[12] A. K. Bertram, A. V. Ivanov, M. Hunter, L. T. Molina, and M. J. Molina, J. Phys. Chem. A **105**, 9415 (2001).

[13] M. J. Molina, A. V. Ivanov, S. Trakhtenberg, and L. T. Molina, Geophys. Res. Lett. **31**, L22104, https://doi.org/10.1029/2004gl020910 (2004).

[14] T. L. Eliason, J. B. Gilman, and V. Vaida, Atmos. Environ. **38**, 1367 (2004).

[15] J. D. Hearn and G. D. Smith, Geophys. Res. Lett. **33**, L17805, https://doi.org/10.1029/2006gl026963 (2006).

[16] Y. Rudich, N. M. Donahue, and T. F. Mentel, Annu. Rev. Phys. Chem. **58**, 321 (2007).

[17] I. J. George and J. P. D. Abbatt, Nat. Chem. **2**, 713 (2010).

[18] F. A. Houle, W. D. Hinsberg, and K. R. Wilson, Phys. Chem. Chem. Phys. **17**, 4412 (2015).

[19] J. E. Hurst, C. A. Becker, J. P. Cowin, K. C. Janda, L. Wharton, and D. J. Auerbach, Phys. Rev. Lett. **43**, 1175 (1979).

[20] C. T. Rettner, E. K. Schweizer, and C. B. Mullins, J. Chem. Phys. **90**, 3800 (1989).

[21] J. Greenwood, Vacuum **67**, 217 (2002).

[22] R. Feres and G. Yablonsky, Chem. Eng. Sci. **59**, 1541 (2004).

18 September 2023 03:06:04

[23] R. M. Logan and R. E. Stickney, J. Chem. Phys. **44**, 195 (1966).

[24] E. K. Grimmelmann, J. C. Tully, and M. J. Cardillo, J. Chem. Phys. **72**, 1039 (1980).

[25] A. Amirav, M. J. Cardillo, P. L. Trevor, C. Lim, and J. C. Tully, J. Chem. Phys. **87**, 1796 (1987).

[26] W. A. Alexander, J. Zhang, V. J. Murray, G. M. Nathanson, and T. K. Minton, Faraday Discuss. **157**, 355 (2012).

[27] D. J. Garton, T. K. Minton, M. Alagia, N. Balucani, P. Casavecchia, and G. Gualberto Volpi, J. Chem. Phys. **112**, 5975 (2000).

[28] D. J. Garton, T. K. Minton, M. Alagia, N. Balucani, P. Casavecchia, and G. G. Volpi, J. Chem. Phys. **114**, 5958 (2001).

[29] J. Harris, *Dynamics of Gas-Surface Interactions (Advances in Gas-Phase Photochemistry and Kinetics)* (Royal Society of Chemistry, 1991), pp. 1–46.

[30] T. Yan, W. L. Hase, and J. R. Barker, Chem. Phys. Lett. **329**, 84 (2000).

[31] T. Yan and W. L. Hase, Phys. Chem. Chem. Phys. **2**, 901 (2000).

[32] T. Yan and W. L. Hase, J. Phys. Chem. B **106**, 8029 (2002).

[33] E. Martínez-Núñez, A. Rahaman, and W. L. Hase, J. Phys. Chem. C **111**, 354 (2007).

[34] J. J. Nogueira, Z. Homayoon, S. A. Vázquez, and E. Martínez-Núñez, J. Phys. Chem. C **115**, 23817 (2011).

[35] J. W. Lu, B. S. Day, L. R. Fiegland, E. D. Davis, W. A. Alexander, D. Troya, and J. R. Morris, Prog. Surf. Sci. **87**, 221 (2012).

[36] E. J. Smoll and T. K. Minton, J. Phys. Chem. C **123**, 22887 (2019).

[37] D. Troya, Theor. Chem. Acc. **131**, 1072 (2012).

[38] P. A. J. Bagot, C. Waring, M. L. Costen, and K. G. McKendrick, J. Phys. Chem. C **112**, 10868 (2008).

[39] C. Waring, K. L. King, P. A. J. Bagot, M. L. Costen, and K. G. McKendrick, Phys. Chem. Chem. Phys. **13**, 8457 (2011).

[40] K. L. King, G. Paterson, G. E. Rossi, M. Iljina, R. E. Westacott, M. L. Costen, and K. G. McKendrick, Phys. Chem. Chem. Phys. **15**, 12852 (2013).

[41] S. L. Lednovich and J. B. Fenn, Am. Inst. Chem. Eng. J. **23**, 454 (1977).

[42] J. A. Faust and G. M. Nathanson, Chem. Soc. Rev. **45**, 3609 (2016).

[43] X.-F. Gao and G. M. Nathanson, Acc. Chem. Res. **55**, 3294 (2022).

[44] H. C. Schewe, B. Credidio, A. M. Ghrist, S. Malerz, C. Ozga, A. Knie, H. Haak, G. Meijer, B. Winter, and A. Osterwalder, J. Am. Chem. Soc. **144**, 7790 (2022).

[45] C. Lee, M. N. Pohl, I. A. Ramphal, W. Yang, B. Winter, B. Abel, and D. M. Neumark, J. Phys. Chem. A **126**, 3373 (2022).

[46] D. J. Nesbitt, A. M. Zolot, J. R. Roscioli, and M. Ryazanov, Acc. Chem. Res. **56**, 700 (2023).

[47] R. H. Bianchini, M. A. Tesa-Serrate, M. L. Costen, and K. G. McKendrick, J. Phys. Chem. C **122**, 6648 (2018).

[48] M. E. Saecker, S. T. Govoni, D. V. Kowalski, M. E. King, and G. M. Nathanson, Science **252**, 1421 (1991).

[49] M. E. King, G. M. Nathanson, M. Hanning-Lee, and T. K. Minton, Phys. Rev. Lett. **70**, 1026 (1993).

[50] M. E. King, M. E. Saecker, and G. M. Nathanson, J. Chem. Phys. **101**, 2539 (1994).

[51] M. E. King, K. M. Fiehrer, G. M. Nathanson, and T. K. Minton, J. Phys. Chem. A **101**, 6556 (1997).

[52] M. E. Saecker and G. M. Nathanson, J. Chem. Phys. **100**, 3999 (1994).

[53] P. D. Lane, K. E. Moncrieff, S. J. Greaves, K. G. McKendrick, and M. L. Costen, J. Phys. Chem. C **124**, 16439 (2020).

[54] B. G. Perkins, T. Häber, and D. J. Nesbitt, J. Phys. Chem. B **109**, 16396 (2005).

[55] B. G. Perkins and D. J. Nesbitt, J. Phys. Chem. B **110**, 17126 (2006).

[56] B. G. Perkins and D. J. Nesbitt, J. Phys. Chem. A **111**, 7420 (2007).

[57] B. G. Perkins and D. J. Nesbitt, Proc. Natl. Acad. Sci. U. S. A. **105**, 12684 (2008).

[58] B. G. Perkins and D. J. Nesbitt, J. Phys. Chem. B **112**, 507 (2008).

[59] B. G. Perkins and D. J. Nesbitt, J. Phys. Chem. A **112**, 9324 (2008).

[60] B. G. Perkins and D. J. Nesbitt, J. Phys. Chem. A **114**, 1398 (2010).

[61] B. G. Perkins, Jr. and D. J. Nesbitt, Phys. Chem. Chem. Phys. **12**, 14294 (2010).

[62] A. Zutz and D. J. Nesbitt, J. Chem. Phys. **147**, 054704 (2017).

[63] T. A. Livingston Large and D. J. Nesbitt, J. Phys. Chem. C **123**, 3449 (2019).

[64] T. A. Livingston Large and D. J. Nesbitt, J. Phys. Chem. C **124**, 28006 (2020).

[65] A. T. J. B. Eppink and D. H. Parker, Rev. Sci. Instrum. **68**, 3477 (1997).

[66] J. R. Roscioli and D. J. Nesbitt, J. Phys. Chem. Lett. **1**, 674 (2010).

[67] D. J. Hadden, T. M. Messider, J. G. Leng, and S. J. Greaves, Rev. Sci. Instrum. **87**, 106104 (2016).

[68] C. H. Hoffman and D. J. Nesbitt, J. Phys. Chem. C **120**, 16687 (2016).

[69] N. Hertl, A. Kandratsenka, O. Bünermann, and A. M. Wodtke, J. Phys. Chem. A **125**, 5745 (2021).

[70] D. J. Harding, J. Neugebohren, H. Hahn, D. J. Auerbach, T. N. Kitsopoulos, and A. M. Wodtke, J. Chem. Phys. **147**, 013939 (2017).

[71] D. J. Harding, J. Neugebohren, D. J. Auerbach, T. N. Kitsopoulos, and A. M. Wodtke, J. Phys. Chem. A **119**, 12255 (2015).

[72] S. P. K. Koehler, Y. Ji, D. J. Auerbach, and A. M. Wodtke, Phys. Chem. Chem. Phys. **11**, 7540 (2009).

[73] R. H. Bianchini, M. J. Roman, M. L. Costen, and K. G. McKendrick, J. Chem. Phys. **151**, 054201 (2019).

[74] M. J. Dyer and D. R. Crosley, Opt. Lett. **7**, 382 (1982).

[75] G. Kychakoff, R. D. Howe, R. K. Hanson, and J. C. McDaniel, Appl. Opt. **21**, 3225 (1982).

[76] Y. Chen, T. Yang, and K. Chen, Phys. Chem. Chem. Phys. **11**, 7111 (2009).

[77] S. Blomberg, J. Zhou, J. Gustafson, J. Zetterberg, and E. Lundgren, J. Phys.: Condens. Matter **28**, 453002 (2016).

[78] E. Fridell, U. Westblom, M. Aldén, and A. Rosén, J. Catal. **128**, 92 (1991).

[79] J. Harris, B. Kasemo, and E. Törnqvist, Surf. Sci. **105**, L288 (1981).

[80] F. Gudmundson, E. Fridell, A. Rosen, and B. Kasemo, J. Phys. Chem. **97**, 12828 (1993).

[81] A. G. Knight, C. Sieira-Olivares, M. J. Roman, D. R. Moon, P. D. Lane, M. L. Costen, and K. G. McKendrick, J. Chem. Phys. **158**, 244705 (2023).

[82] D. R. Miller, in *Atomic and Molecular Beam Methods: Volume 1,* edited by G. Scoles (Oxford University Press, 1988), pp. 14-53.

[83] U. Stopper, P. Lindner, and U. Schumacher, Rev. Sci. Instrum. **78**, 043508 (2007).

[84] J. Luque and D. R. Crosley, SRI International Report No. MP, 99, 1999.

[85] D. van der Spoel, E. Lindahl, B. Hess, G. Groenhof, A. E. Mark, and H. J. C. Berendsen, J. Comput. Chem. **26**, 1701 (2005).

[86] H. J. C. Berendsen, D. van der Spoel, and R. van Drunen, Comput. Phys. Commun. **91**, 43 (1995).

[87] W. L. Jorgensen, D. S. Maxwell, and J. Tirado-Rives, J. Am. Chem. Soc. **118**, 11225 (1996).

[88] J. E. Black, G. M. C. Silva, C. Klein, C. R. Iacovella, P. Morgado, L. F. G. Martins, E. J. M. Filipe, and C. McCabe, J. Phys. Chem. B **121**, 6588 (2017).

[89] C. Klein, A. Z. Summers, M. W. Thompson, J. B. Gilmer, C. McCabe, P. T. Cummings, J. Sallai, and C. R. Iacovella, Comput. Mater. Sci. **167**, 215 (2019).

[90] J. Zhang, D. J. Garton, and T. K. Minton, J. Chem. Phys. **117**, 6239 (2002).

[91] T. Pradeep, S. A. Miller, and R. G. Cooks, J. Am. Soc. Mass Spectrom. **4**, 769 (1993).

[92] S. Ramasamy and T. Pradeep, J. Chem. Phys. **103**, 485 (1995).

[93] V. Bindu, K. Smitha, and T. Pradeep, Mol. Phys. **93**, 85 (1998).

[94] P. D. Lane, S. J. Greaves, M. L. Costen, and K. G. McKendrick, "A molecular dynamics study of the gas-liquid interfaces of PFPE, squalane, and squalene" (unpublished).

[95] U. Tasić and D. Troya, Phys. Chem. Chem. Phys. **10**, 5776 (2008).

[96] W. A. Alexander, J. R. Morris, and D. Troya, J. Chem. Phys. **130**, 084702 (2009).

[97] M. L. Costen, S. Marinakis, and K. G. McKendrick, Chem. Soc. Rev. **37**, 732 (2008).